analytical chemistry

pubs.acs.org/ac Article

Precise Electron-Withdrawing Strength Modulation of ESIPT Probes for Ultrasensitive and Specific Fluorescence Sensing

Yanwen Guo, Zhenzhen Cai,* Fei Yan, Da Lei, Yanan Guo, Shuhai Zhang,* and Xincun Dou*

Cite This: *Anal. Chem.* 2023, 95, 9014−9024 Read Online

ACCESS | Metrics & More | Article Recommendations | Supporting Information

ABSTRACT: The precise regulation of the electron-withdrawing/electron-donating strength in a probe is of great significance for the design of reaction-based fluorescent probes with specific functionalities. Here, a family of excited-state intramolecular proton transfer (ESIPT)-based probes with fluorescence turn-on sensing properties toward $KMnO_4$ was designed by precisely modulating the electron-withdrawing strength of the substituents located at the *para*-position of the recognition group. It is found that −F, −CHO, and −H as the electron-withdrawing groups bound at the probe can specifically recognize $KMnO_4$, which ensures a blue emission displayed by the reaction products. Especially with −CHO as the electron-withdrawing group, the reaction product shows the most stable fluorescence. The probe 2-(benzo[*d*]oxazol-2-yl)-4-formylphenyl acrylate (BOPA-CHO) demonstrated a more superior sensing performance toward $KMnO_4$, including a low limit of detection (LOD, 0.96 nM), a rapid response (<3 s), and a rather good selectivity even in the presence of 21 interferents. Moreover, the practicality of the probe was further verified by a test pen comprising a BOPA-CHO-embedded sponge, which is capable of detecting $KMnO_4$ solid with a naked-eye LOD of 11.62 ng. The present probe design and modulation strategy would open up a new path for the design of high-performance fluorescent probes.

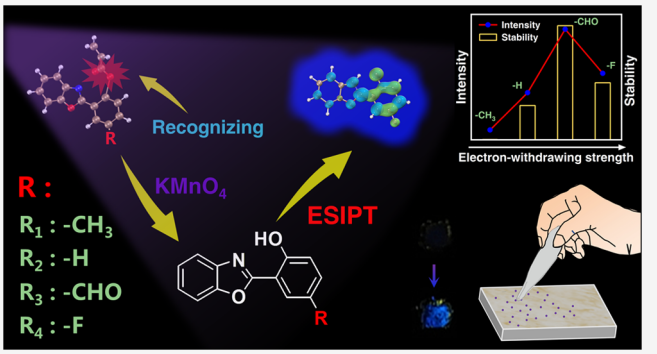

Understanding the molecular interactions in chemical systems is the heart of chemistry.[1−3] Chemical probes, including small-molecules,[4−6] metal−organic frameworks,[7,8] fluorescent quantum dots,[9−11] and nanoclusters,[12−15] widely used as diagnostic, monitoring, and analytical tools in biochemical, medical, and environmental fields as well as industry,[16−22] provide useful means for investigating the molecular interactions. Among them, organic small-molecule fluorescent probes have been developed based on receptor−analyte noncovalent interactions or irreversible chemical reactions and possess the advantages of adjustable structures, fast response, high luminous efficiency, and ease of operation, which have drawn considerable attention.[23−25] Reaction-based fluorescent probes provide higher selectivity with larger spectroscopic changes than fluorescent probes based on noncovalent interactions in most cases, owing to the structural changes from the formation or breaking of the covalent bonds.[26−28] The excited-state intramolecular proton transfer (ESIPT) science has been widely investigated and shows extremely important significance in the field of displaying,[29,30] imaging,[31] lasing,[32] and sensing.[33,34] In the field of sensing, as one of the most basic strategies for designing reaction-based fluorescent probes, ESIPT possesses remarkable properties, such as a large Stokes shift, enhanced photostability, ultrafast process, and spectral sensitivity to the surrounding medium, and has been extensively investigated on the design strategies, detailed photophysical properties, and promising applications.[35−37] In general, the prerequisite for ESIPT is the presence of an intramolecular hydrogen bond between the proton donor (−OH and $-NH_2$) and the proton acceptor (=N− and −C=O) groups in close proximity to each other in a probe. The general strategy for the development of reaction-based ESIPT fluorescent probes is based on blocking the hydrogen bond donor of the ESIPT fluorophore with a reactive unit that prevents the ESIPT process. While exposing the probes to a specific analyte, exchangeable protons are available, which results in the occurrence of the ESIPT process. The sensing performance of ESIPT fluorescent probes is mainly affected by the spectral properties of the fluorophores, which can be modulated by the hydrogen bonding,[38,39] isomerization process,[40] acidity/basicity of the surrounding medium,[41] and chemical modifications[39] on the probes. Among them, the chemical modifications, including π-extensions and substituent groups with electron-donating/electron-withdrawing groups

Received: March 13, 2023
Accepted: May 22, 2023
Published: June 1, 2023

on either or both proton donor moieties, such as the hydroxyphenyl ring, etc., and proton acceptor moieties, such as benzothiazole, benzoxazole, benzimidazole, etc., have attracted considerable attention to investigate the process of ESIPT, which can change the intramolecular hydrogen bond strength and the energy barrier, thus hindering or promoting the occurrence of the ESIPT process.[32,33,42,43] However, most of these chemical modification strategies focused on the molecular properties and the ESIPT process change from the perspective of theoretical analysis and still lack a systematical investigation regarding how and to which extent the regulation of the probe structure would affect the ESIPT luminescence process and the resulting sensing performance toward the target analyte. Furthermore, it has rarely been applied in practical detection, which should be predominantly due to the challenge of experimentally observing the molecular structure changes in the ESIPT process. Hence, whether a chemical modification strategy could be employed to improve the sensing performances of the ESIPT probe remains unknown but is of great significance for the rational design of highly efficient probes.

Potassium permanganate ($KMnO_4$), as a powerful oxidant, is widely used in chemical production, water purification, and wastewater treatment.[44−46] In the latest release of sanitary standards for drinking water, the limit of MnO_4^- has been adjusted to 3 mg/L (0.025 mM). On the one hand, its massive discharge can cause severe environmental pollution and excessive intake can lead to irreversible organ necrosis,[47] and on the other hand, it is one of the most frequently used raw materials in preparing improvised explosives.[48−50] Hence, the rapid and highly sensitive identification of trace $KMnO_4$ is of great significance for environmental and safety requirements. To achieve accurate, rapid trace detection of $KMnO_4$, the commonly used optical detection method is based on the inner filter effect (IFE),[51,52] which generates fluorescence turn-off responses.[53−55] However, this method suffers from low selectivity, sensitivity, and response speed, owing to the detection mechanism of the probes and the absorption nature of $KMnO_4$, which limits its application in actual environments.[56] The fluorescence-on detection of $KMnO_4$ is mainly based on the mechanisms of charge transfer (CT),[57] cation luminescence,[47] and twisting intramolecular charge transfer.[45] Although these methods have good anti-interference to complex environments, some oxidizing substances still have a certain amount of interference. Another choice for detecting $KMnO_4$ is based on common sense by employing the unsaturated double bond as the recognition site through the oxidative cracking mechanism.[45,46] However, it has been demonstrated that other oxidants, such as H_2O_2 and $K_2Cr_2O_7$ can also oxidize the double bond despite their oxidation capability differences.[58] Whether a new fluorescence-on probe design strategy with high sensitivity, anti-interference, and rapid and trace detection performance toward $KMnO_4$ could be developed based on the efficient employment of the double bond is full of challenges but is attractive enough considering the pressing demand either in environmental monitoring or in public security maintaining.

To this end, a series of ESIPT fluorescent probes based on 2-(2′-hydroxyphenyl) benzoxazole (HBO) by precisely modulating the electron-withdrawing strength of the substituents located at the *para*-position of the recognition group were designed and synthesized to realize the rapid and fluorescence-on detection of $KMnO_4$ with high sensitivity, anti-interference, and optical stability. It is revealed that a stronger electron-withdrawing capability would greatly facilitate the increase of the reactivity of the recognition site. Taking into account the fluorescence emission intensity and the stability of the product after the reaction with $KMnO_4$, the probe BOPA-CHO was proved to be the most efficient probe. The fast fluorescence turn-on behavior of the probe enables a low detection limit (0.96 nM), a stable fluorescence within a tested time range of 7 days, and a perfect specificity facing 21 types of oxidants and common anions or cations. The present probe modulation strategy was further validated by incorporating the probe in a sponge-based test pen for practical scenario applications with ultrasensitive recognition capability toward ng-level $KMnO_4$ particles.

EXPERIMENTAL SECTION

Materials and Characterization. Unless otherwise noted, all reagents and materials were obtained from commercial sources, and all were used without further purification. Polyphosphoric acid (PPA), 2-aminophenol, triethylamine (Et_3N), acryloyl chloride, 5-fluoro-2-hydroxybenzoic acid, 5-formylsalicylic acid, salicylic acid, and 5-methylsalicylic acid were purchased from Aladdin Chemical Reagent Co., Ltd. All of the organic solvents such as tetrahydrofuran (THF), petroleum ether (PE), ethyl acetate (EA), dichloromethane (DCM), and inorganic salts were bought from Sinopharm Chemical Reagent Co., Ltd. Solvents used for synthesis and optical property characterization were of analytical grade and chromatographic grade, respectively.

Using tetramethylsilane (TMS) as an internal standard, ^1H NMR and ^{13}C NMR spectra were measured on a Varian high-resolution 400 MHz superconducting NMR spectrometer. Mass spectra of fluorescent probes and products were determined with a Q Exactive-type four-stage rod-Orbitrap high-resolution mass spectrometer (HRMS, UHPLC-Q-Orbitrap-HRMS, Thermo Fisher Scientific). Ultraviolet−visible absorption spectra were measured on a Hitachi UV-3900 ultraviolet−visible spectrophotometer, and fluorescence spectra were measured on an Edinburgh FLS1000 fluorescence spectrophotometer. A grating spectrometer (Maya 2000 Pro) of ocean optics was used to measure the time-dependent spectral characteristics. Attenuated total reflection Fourier transform infrared (ATR-FTIR) spectra and Fourier transform infrared (FTIR) spectra were obtained using a Frontier thermogravimetric infrared analysis system (PerkinElmer). The optical micrographs and videos were recorded on a MERCURY GigE Camera (MER-2000-5GC).

Synthesis Process of Probes. Polyphosphoric acid (20 mL), 2-aminophenol (6 mmol), and 5-fluoro-2-hydroxybenzoic acid or 5-formylsalicylic acid or salicylic acid or 5-methylsalicylic acid (6 mmol) were mixed in a triple-necked flask and stirred overnight at 180 °C. The crude product was precipitated from the viscous solution by adding ice water. An intermediate product was obtained by column chromatography. Then, the intermediate products (0.25 mmol), Et_3N (1.125 mmol), and DCM (10 mL) were mixed in a flask and stirred in an ice bath. The acryloyl chloride (0.75 mmol) was added dropwise. After 30 min, the reaction was stirred at room temperature for 12 h. Finally, the probe was obtained by dilution, washing, drying, and column chromatography.

Preparation and Testing of the BOPA-CHO-Embedded Sponge-Based Test Pen for the Analyte. The shell of the test pen was prepared by 3D printing technology, and a

https://doi.org/10.1021/acs.analchem.3c01120
Anal. Chem. 2023, 95, 9014−9024

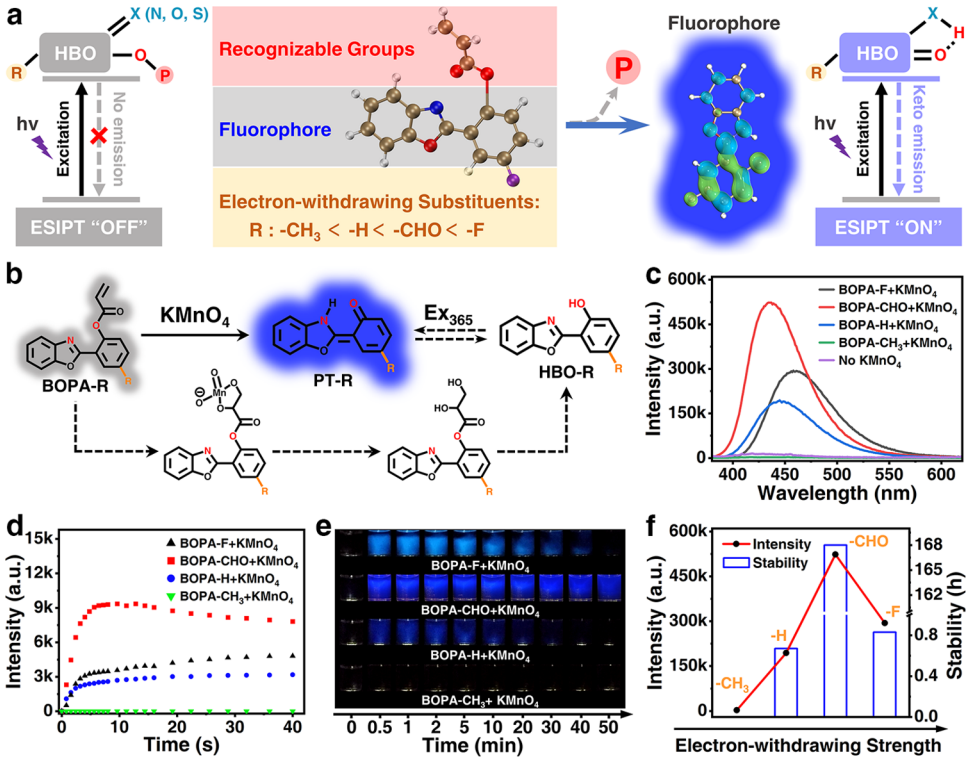

Figure 1. (a) Schematic diagram of the design strategy of an ESIPT-based probe and the precise regulation of the substituent groups' electron-withdrawing strength bound at the *para*-position of the recognition site. (b) Proposed detection mechanism of the BOPA-based probe for recognizing $KMnO_4$. (c) Fluorescence emission spectra of the four probes before and after detecting $KMnO_4$. (d) Corresponding time-dependent fluorescence response of these probes after adding $KMnO_4$. (e) Time-lapse images extracted from the videos of the BOPA-based probes detecting $KMnO_4$ captured using a digital camera. (f) Corresponding relationship between the fluorescence emission intensity and the fluorescence stability of the BOPA-based probes in response to $KMnO_4$ with respect to the substituent groups' electron-withdrawing strength.

BOPA-CHO-embedded sponge-based sensing unit was placed on the tip of the pen to obtain the test pen. When detecting the analyte, the test pen gently wiped the residual sample for sampling, and the fluorescence change of the pen tip was observed under the irradiation of a 365 nm ultraviolet lamp.

RESULTS AND DISCUSSION

Modulation of Electron-Withdrawing Strength on the Probe Detection Performance. Based on the luminescence mechanism of ESIPT, a reaction-based fluorescent probe design strategy was proposed to improve the detection performance of the analyte by regulating the electron-withdrawing strength of the substituents, which was located at the *para*-position of the recognition groups (Figure 1a). HBO, as a typical ESIPT fluorophore, was widely applied in probe design in biological systems.[59] Here, it was used to construct a reaction-based probe by linking the recognition site to the proton donor and introducing different electron-withdrawing groups in the *para*-position of the recognition site to modulate its reactivity.

Probes with the acryloyl group as the recognition site have been reported for the detection of biological thiols,[60,61] but the effect of substituent regulation on sensing performance has not been researched. A series of probes (BOPA-F, BOPA-CHO, BOPA-H, BOPA-CH_3) were designed and synthesized by linking the acryloyl group to the proton donor of HBO as the recognition site of $KMnO_4$ based on the condensation reaction to prevent the ESIPT process, and different electron-withdrawing groups (−F, −CHO, −H, $-CH_3$) were introduced in the *para*-position of the acryloyl group (Scheme S1 and Figures S1−S28). As a result, these probes have no fluorescence under photoexcitation because no exchangeable protons are available. Once $KMnO_4$ reacts with the unsaturated double bond of the acryloyl group, the acryloyl group would be oxidized to form 2,3-dihydroxypropyl, and then the ester group could be hydrolyzed, followed by the release of the proton donor and formation of HBO-F, HBO-CHO, HBO-H, and HBO-CH_3. Under photoexcitation, the ESIPT process could be triggered, the charge of the product would redistribute, and the structure would be converted into ketone isomers (PT-F, PT-CHO, PT-H, PT-CH_3), which show fluorescence emission (Figure 1b). The structure of these products is firmly evidenced by nuclear magnetic resonance (NMR) and high-resolution mass spectroscopy (HRMS). From the ^{1}H NMR spectra, the chemical shifts at 6.0−7.0 ppm corresponding to the acryloyl group of the probes disappear and a new proton signal attributed to the hydroxyl appears at near 11 ppm (Figures S29 and S30). From the ^{13}C NMR spectra, one can see that the signal at near 128 ppm corresponding to the carbon atom of the acryloyl group disappeared (Figures S31 and S32). Meanwhile, the HRMS data show that after the addition of $KMnO_4$, the peaks at m/z 284.07 and 294.08 corresponding to BOPA-F and BOPA-CHO disappeared, and two new peaks at m/z 230.06 and 240.07 corresponding to the reaction products appeared (Figures S33 and S34). In addition, the UV−vis absorption spectra and the corresponding optical images of the BOPA-based probes toward $KMnO_4$ were evaluated, respectively (Figure S35). The color of the probe solution changing from colorless to pale yellow after the addition of $KMnO_4$ could be

https://doi.org/10.1021/acs.analchem.3c01120
Anal. Chem. 2023, 95, 9014−9024

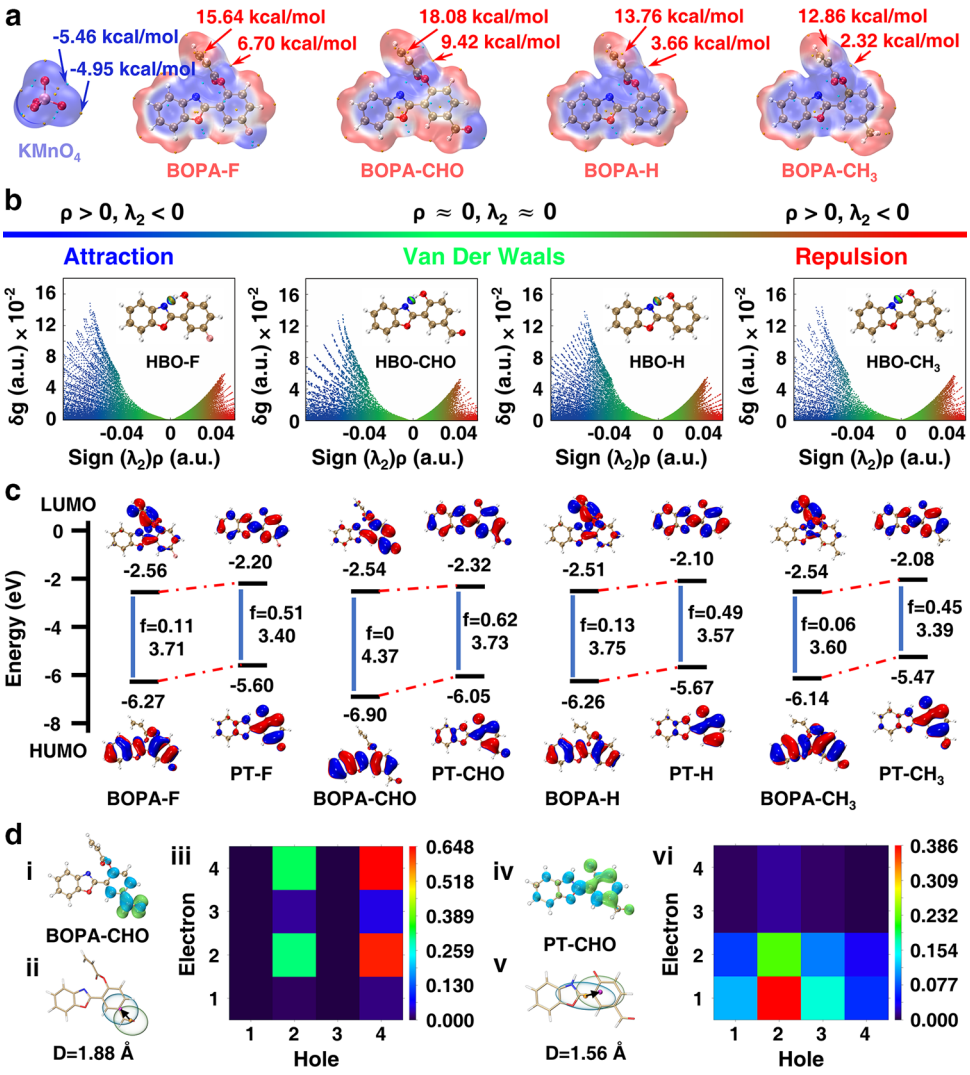

Figure 2. (a) Electrostatic potential distribution diagrams of the $KMnO_4$ and four probes. (b) Scatter pattern and isosurface of the noncovalent interaction of the probe reaction products and solvent in the molecule, respectively. The δg reflects the interaction strength, and the sign $(\lambda_2)\rho$ reflects the interaction type with different colors. (c) Electron-density distribution and the corresponding energy diagrams of the main molecular orbitals of the probes and their photoexcited reaction products, respectively. Red and blue regions denote the positive and negative orbital phases, respectively. (d) (i), (iv) Hole and electron distributions; (ii), (v) C_{hole}/C_{ele} maps smoothly transformed from hole and electron distributions; and (iii), (vi) the fragment transition density matrix maps of the probe BOPA-CHO and the excited product PT-CHO, and the centroids of C_{hole} and C_{ele} were, respectively, marked by the purple and orange spheres.

ascribed to the reductive product of $KMnO_4$, accompanied by a new maximum absorption around 290 nm. These results clearly proved the reasonability of the proposed probe design strategy.

To gain a high sensing performance, the mixture of THF and H_2O with a volume ratio of 1:4 was determined as the reaction solvent (Figure S36). It should be noted that this ratio was optimized by considering the most pronounced detection phenomenon and the dissolving function of the target analytes. It is clear that the four probes show no fluorescence emission (Figures 1c and S37). Upon the addition of $KMnO_4$, the fluorescence of the probes BOPA-F, BOPA-CHO, and BOPA-H were turned on, and the emission peaks appeared at 458, 434, and 445 nm, respectively, while no fluorescence change was observed in probe BOPA-CH_3. The time-dependent fluorescence intensities observed at the optimal emission peaks were recorded to evaluate the response time and stability of the probes toward $KMnO_4$, respectively (Figure 1d). The fluorescence intensities of probes BOPA-F, BOPA-CHO, and BOPA-H rapidly increased to more than 50% of the maximum value within 3 s, and then the probe BOPA-CHO reached the maximum value in 5 s and decreased slightly and remained relatively stable afterward. The intensities of probes BOPA-F and BOPA-H increased slightly and then remained stable after 30 s. To further investigate the stability of the reaction products of BOPA-based probes toward $KMnO_4$, the changing of the fluorescence with time was recorded by taking optical pictures under irradiation with a 365 nm UV lamp (Figure 1e). It can be observed that the fluorescence intensity of product HBO-CHO almost did not change within 50 min. A further test shows that the HBO-CHO still has strong fluorescence emission after 7 days (Figure S38). However, the fluorescence of products HBO-F and HBO-H gradually weakened at 5 min and then completely disappeared at 50 min or 40 min, which verifies well the feasibility of the probe design strategy with a stable luminescence to facilitate the practical application.

https://doi.org/10.1021/acs.analchem.3c01120
Anal. Chem. 2023, 95, 9014−9024

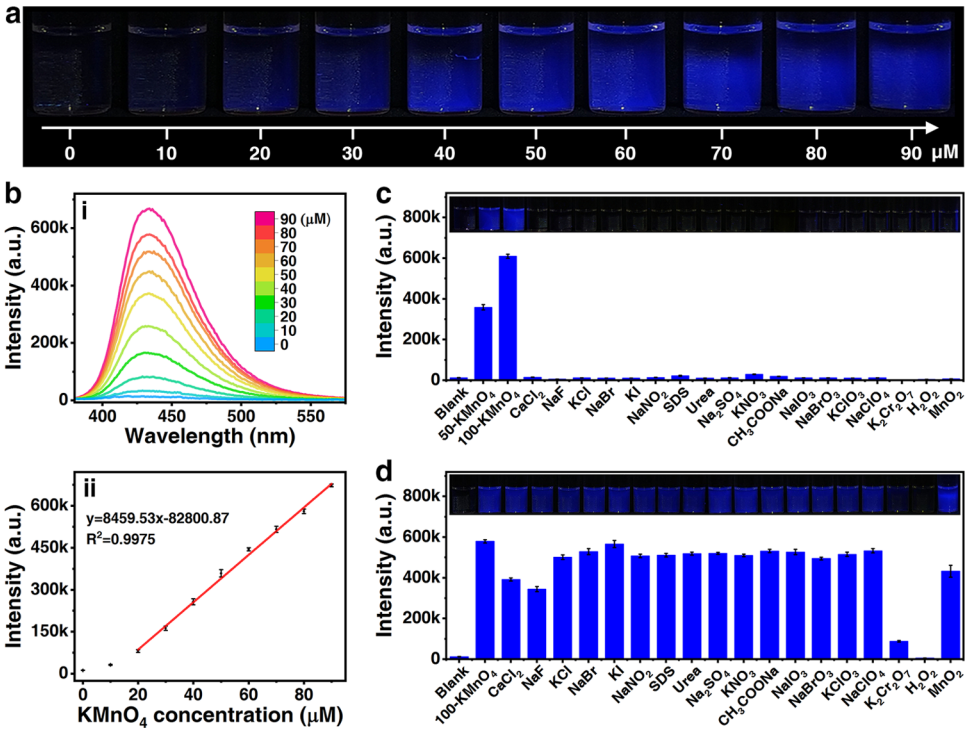

Figure 3. Fluorescence response and specificity of the probe BOPA-CHO. (a) Optical images, and (b) (i) fluorescence spectra of the probe in response to different concentrations of $KMnO_4$ (0−90 μM), and (ii) emission intensity at 434 nm as a function of $KMnO_4$ concentration. Emission intensity at 434 nm changes obtained for the probe in response to (c) various analytes (1 mM) and $KMnO_4$ (50 and 100 μM), and (d) a mixture of $KMnO_4$ (100 μM) and various analytes (1 mM). The excitation wavelength is 365 nm, and the standard deviations were obtained from three repeated measurements.

Thus, with the enhancement of the electron-withdrawing strength of the substituents, the fluorescence intensity and fluorescence stability of the HBO-based products generally increase (Figure 1f). However, although −F has the strongest electron-withdrawing strength, the fluorescence intensity and stability of BOPA-F are weaker than those of BOPA-CHO. It is considered that due to the strong hydrogen bond between −F and the solvent, the intramolecular proton transfer in HBO-F was weakened, which inhibits the ESIPT process. As a result, the strength of the electron-withdrawing groups linked in the *para*-position of the proton donor would greatly affect the reactivity of the probe, the fluorescence intensity, and the stability of the product, and probe BOPA-CHO is proved to be the most efficient one among these modulated probes.

Role of Electron-Withdrawing Strength in Probe Reactivity. First, the electrostatic potential (ESP) surfaces of the probes were investigated by the natural bond orbital method in order to explore the factors causing the difference in fluorescence response of different probes to $KMnO_4$ (Figure 2a). It can be seen that ESP values of the $KMnO_4$ are all negative (cyan region), indicating that it is nucleophilic and easier to attack the electron-deficient position of the probe. Similarly, the ESP of the four probes is positive near the C═C bond and the ester bond (orange region), and the maximum value is located near the C═C reaction with the probe. By comparing ESP values of the four probes near the C═C bond, it is found that BOPA-CHO has the maximum value (18.08 kcal/mol), followed by BOPA-F (15.64 kcal/mol), BOPA-H (13.76 kcal/mol), and BOPA-CH_3 (12.86 kcal/mol), indicating that the nucleophilicity of $KMnO_4$ to these four probes gradually decreases. This electrostatic potential result is very consistent with the experimental results on the reactivity of the probes.

The intramolecular noncovalent interactions of the reaction products in the solvent were analyzed using the independent gradient model (IGM), respectively (Figure 2b). It can be seen that the density of different colors of scatter represents the strength of different noncovalent interactions. Obviously, the hydrogen bond is the main force (blue scatter) within the four probe products, and the intensity follows HBO-CH_3 > HBO-F > HBO-H > HBO-CHO. This can also be intuitively illustrated by topological analysis of atoms in molecules (AIM) of intramolecular hydrogen bonds, potential energy density, and bond energy of probe reaction products (Table S1). The smaller the bond length, the larger the potential energy density, and the larger the absolute value of the bond energy, the stronger the intramolecular hydrogen bond. With a stronger intramolecular hydrogen bond, the proton transfer will be more easily induced in the excited state, which would be more favorable for the ESIPT process to form ketone isomers. This result clearly shows that all these four products can transfer protons under photoexcitation.

To analyze the HOMO and LUMO energy levels and oscillator strength changes of the probes before and after the detection of $KMnO_4$, the molecular orbital theory was employed (Figure 2c). Taking the case of the probe BOPA-F, its HOMO/LUMO electron transition energy is 3.71 eV, and its HOMO/LUMO electron cloud density shifts obviously, resulting in a low oscillator strength at 445 nm (f = 0.11) with no fluorescence emission (Figure S39 and Table S2). While after the reaction with $KMnO_4$, the HOMO/LUMO electron transition energy of the excited product PT-F is 3.40 eV, which decreased by 0.31 eV compared with that

https://doi.org/10.1021/acs.analchem.3c01120
Anal. Chem. 2023, 95, 9014−9024

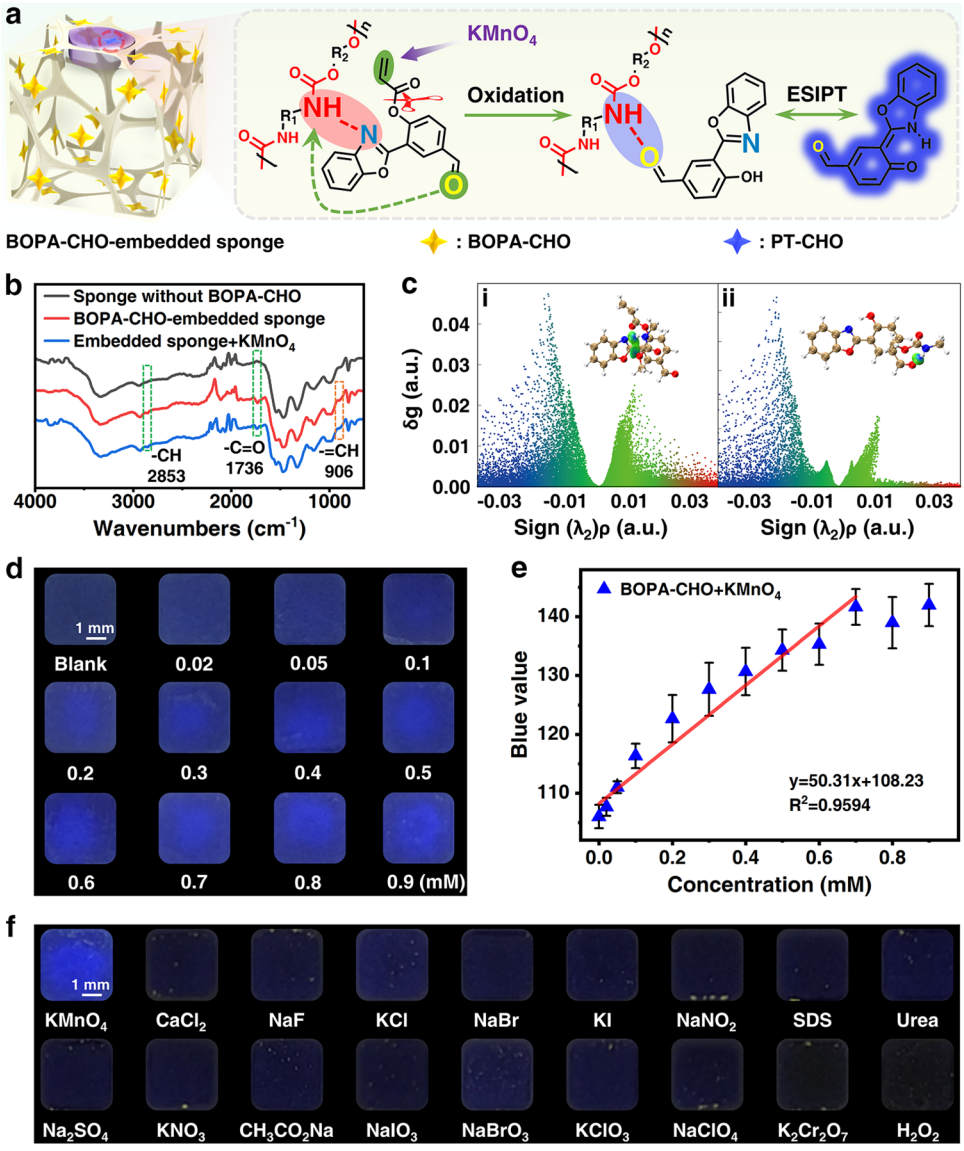

Figure 4. (a) Schematic illustration of the construction of the BOPA-CHO-embedded sponge sensor unit and the fluorescence detection of $KMnO_4$ solution. (b) ATR-FTIR spectra of the polyurethane-based sponges and the BOPA-CHO-embedded sponges before and after detection of $KMnO_4$. (c) Scatter graph and isosurface of noncovalent interactions between the polyurethane-based sponge and (i) the probe BOPA-CHO and (ii) the product HBO-CHO, respectively. (d) Fluorescence images of the BOPA-CHO-embedded sponge sensor unit before and after detecting $KMnO_4$ (0−0.9 mM). (e) Corresponding blue values of the fluorescence images in panel (d) as a function of the concentration of $KMnO_4$. (f) Selective fluorescence images of the BOPA-CHO-embedded sponge sensor unit.

before the reaction, consistent with the red shift in the spectra. Meanwhile, the electron cloud of PT-F overlapped in space, and a strong oscillator strength (f = 0.51) was generated at 464 nm, consistent with the presented strong fluorescence emission. The other three probes have similar HOMO and LUMO energy levels and oscillator strength despite different values. Probe BOPA-CHO has the largest change of electron transition energy (0.64 eV) and oscillator strength (f = 0.62), which is considered to be the reason why the corresponding fluorescent product is much more stable. It should be noted that although from the view of the change of energy levels, the PT-CH_3 can also emit fluorescence, it cannot be formed in real cases due to the low reactivity resulting from the weak electron-withdrawing strength of $-CH_3$. The hole−electron analysis of probe BOPA-CHO showed that although the hole and electron distributions overlapped in the vicinity of the aldehyde group, they were obviously separated in general, showing green and blue regions (Figure 2d(i)). The distance (D) of the electron excitation from the hole distribution center (C_{hole}) to the electron distribution center (C_{ele}) is 1.88 Å (Figure 2d(ii)). In addition, the probe was divided into four fragments to obtain the heat map of the fragment transition density matrix (Figures 2d(iii), S40, and S41). It can be seen that the hole distribution on the X-axis is mainly concentrated in fragment 4, showing an obvious red color, and there are also some holes in fragment 2, while the electron distribution on the Y-axis is mainly concentrated in fragment 2 and fragment 4, implying that some electrons are transferred from segment 4 to segment 2. The reason why the probe BOPA-CHO has no fluorescence could be attributed to the large overlapping of the transition dipole moment distribution (Figure S42). In contrast, the hole and electron distributions of the PT-CHO near the oxazole ring highly overlap, and the D value is 1.56 Å (Figure 2d(iv),(v)). The hole distribution is mainly concen-

https://doi.org/10.1021/acs.analchem.3c01120
Anal. Chem. 2023, 95, 9014−9024

trated in fragment 2, and the electron distribution is concentrated in fragments 1 and 2 (Figure 2d(vi)), implying that there are electrons transferring from fragment 2 to fragment 1, which is the origin of the fluorescence.

Fluorescence Detection and Discrimination of $KMnO_4$. To systematically investigate the detection performance of the probe BOPA-CHO, a series of $KMnO_4$ solutions with concentrations up to 90 μM were tested (Figure 3a). From the fluorescence images of the probe toward $KMnO_4$ under irradiation with a 365 nm UV lamp, it can be seen that the dark blue fluorescence becomes brighter and brighter with the increase of the $KMnO_4$ concentration. In particular, a concentration of 10 μM $KMnO_4$ can be visually distinguished. From the corresponding fluorescence spectra, one can see that the emission peak centered at 434 nm gradually increases with the increase of the concentration of $KMnO_4$ (Figure 3b(i)). Accordingly, the emission intensity at 434 nm as a function of the $KMnO_4$ concentration was plotted (Figure 3b(ii)). It can be seen that the emission intensity slowly increases when the $KMnO_4$ concentration is below 20 μM and rapidly increases with the further increase of the $KMnO_4$ concentration. To further investigate the detection performance of the probe, the emission intensity with respect to the $KMnO_4$ concentration in the range of 20−90 μM was fitted linearly. Thus, the limit of detection (LOD, defined as LOD = $3\sigma/k$, where k = 8459.53 is the slope of the linear part of the calibration curve, and σ = 3 is the standard deviation of noise) of the probe toward $KMnO_4$ was calculated to be 0.96 nM, which is among the most superior LODs compared with the other probes reported previously (Table S3), verifying the advantages of the proposed probe design strategy.

To investigate the selectivity of the probe BOPA-CHO toward $KMnO_4$, 21 kinds of interferents, including oxidants and common anions and cations, and other ions found in environmental water systems were selected (Figures 3c, S43a, and S44). Upon the addition of various interferents (1 mM) into the probe solution, the fluorescence images and intensities show negligible changes, which is in sharp contrast with the bright fluorescence when different concentrations of $KMnO_4$ (50 and 100 μM) were added, respectively. It should be noted that other strong oxidants, including KNO_3, $NaIO_3$, $NaBrO_3$, $KClO_3$, $NaClO_4$, $K_2Cr_2O_7$, and H_2O_2, could not cause the breaking of the unsaturated double bond in the probe. It is further demonstrated that the individual mixing of these interferents (1 mM) except $K_2Cr_2O_7$, H_2O_2, and $FeCl_3$ into $KMnO_4$ (100 μM) would not obviously disturb the judge of the existence of $KMnO_4$ since the intensity is always maintained at more than 60% of that with pure addition of $KMnO_4$ (Figures 3d, S43b, and S45). It is considered that the coexistence of H_2O_2 with a high concentration would reduce $KMnO_4$ completely, and $K_2Cr_2O_7$ and $FeCl_3$ could absorb the excitation of PT-CHO (Figure S46).

BOPA-CHO-Embedded Sponge Sensor Unit for $KMnO_4$ Solution Detection. To further enhance the detection capability of the BOPA-CHO probe toward $KMnO_4$ solution, an integrated elastic BOPA-CHO-embedded polyurethane sponge sensor unit with no fluorescence emission was fabricated (Figure 4a). This device design originates from two aspects, the first one is to restrain the dispersion of the target analyte solution and thus boost the sensitivity compared to the free-diffusion solution system, and the other one is to ensure the efficient anchoring of the probe through the NH−N interaction and the occurrence of the intrinsic ESIPT process of the HBO-CHO with the release of the =N−. The embedding of the probe BOPA-CHO into the polyurethane-based sponge could be evidenced by the appearance of the stretching vibrations of −C=O and −C−H at 1736 and 2853 cm^{-1}, respectively, in the ATR-FTIR spectra (Figure 4b). In addition, the weakening of the stretching vibration peak at 906 cm^{-1} after the reaction with $KMnO_4$ proves the reduction of =CH. Moreover, to investigate the interaction between polyurethane and the probe as well as the reaction product, the independent gradient model (IGM) was employed. It is shown that there is a strong hydrogen bond (blue region) between the =N− in the probe and the −NH− in the polymer chain (Figure 4c(i)). However, after the reaction with $KMnO_4$, this hydrogen bond shifted to the bonding between −NH− and −C=O in the product (Figures 4c(ii) and S47), which confirmed that the H-proton in the HBO-CHO could transfer from the hydroxyl group to the oxazole ring, providing a prerequisite for the occurrence of the ESIPT process. In addition, the discrete points in the scatter graphs of the two clusters show a similar pattern with spikes around the negative sign $(\lambda_2)\rho$ (−0.02) and high δg (>0.045), confirming the strong attraction between −NH− and =N− or −C=O.

The detection performance of the sensor unit toward $KMnO_4$ solution was investigated (Figure 4d). Upon addition of 3 μL of $KMnO_4$ solution with concentrations of 0.02−0.9 mM onto the unit, the solution rapidly diffused into the sponge, and a blue fluorescence could be observed, and the emission gradually became bright upon increasing the concentration of $KMnO_4$. It is worth noting that compared with the aforementioned free-diffusion liquid detection, the unit shows a much more significant fluorescence turn-on performance with a trace amount of the analyte (3 μL) when detecting the same concentration of $KMnO_4$ solution. Specifically, the $KMnO_4$ solution with a concentration of 0.02 mM can also be obviously detected, which is below the national sanitation standards for drinking water. It further proves that the polyurethane sponge is an appropriate sensing substrate to ensure the efficient detection of trace $KMnO_4$ solution through the ESIPT process. The fluorescence changes were further analyzed by extracting the average blue values of the images and plotting them as a function of the concentration of $KMnO_4$ (Figure 4e). It can be observed that the changing trend for detecting $KMnO_4$ is highly consistent with the naked-eye observation. Furthermore, the blue values of the images increase linearly in the presence of $KMnO_4$ solution with an ascending concentration from 0 to 0.7 mM, indicating that the sponge sensor unit could achieve quantitative sensing to a certain extent. To avoid the interference of common solvents on the detection performance of the sensor unit, 17 types of interferents in the liquid form were selected for comparison (Figure 4f). From the fluorescence images, it can be seen that blue fluorescence only appeared when detecting $KMnO_4$, and all of the interferents showed a negligible fluorescence change. This result further proved that the BOPA-CHO-embedded sponge sensor unit is highly reliable for the practical detection of trace $KMnO_4$ solution.

BOPA-CHO-Embedded Sponge-Based Test Pen for $KMnO_4$ Residue Detection. Currently, the practical detection of $KMnO_4$ mainly focuses on the analysis of the solution samples in industrial sewage,[62,63] biological cells,[54,64,65] aquaculture,[66] etc. To further prove the applicability of the proposed BOPA-CHO probe for the rapid, on-

https://doi.org/10.1021/acs.analchem.3c01120
Anal. Chem. 2023, 95, 9014−9024

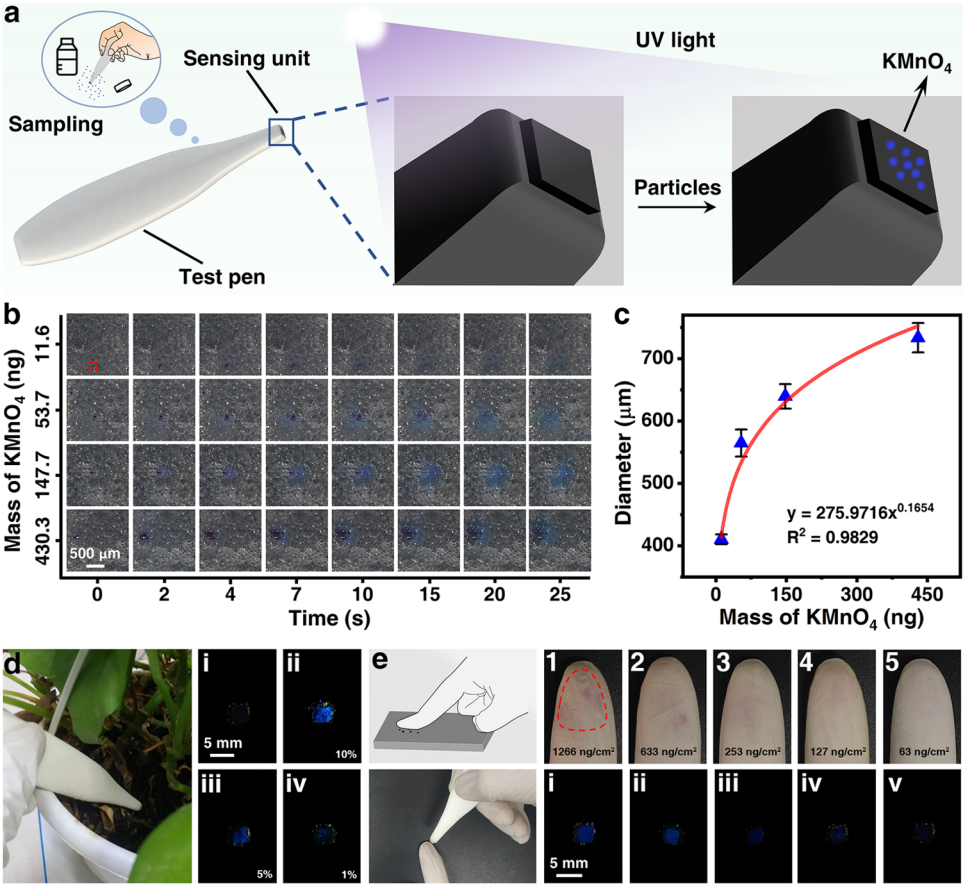

Figure 5. (a) Schematic illustration of the structure of a BOPA-CHO-embedded sponge-based test pen and the fluorescence change toward $KMnO_4$ particles. (b) Time-lapse images extracted from the video of the sensing process captured under an industrial camera. (c) Relationship between the diffusion diameter at 25 s and the mass of the $KMnO_4$ particles. Practical fluorescence detection of the test pen for (d) $KMnO_4$-contaminated soil and (e) trace amounts of $KMnO_4$ residues on gloves.

site detection of trace $KMnO_4$, a BOPA-CHO-embedded sponge-based test pen was constructed (Figure 5a). Real-time detection images for different masses of $KMnO_4$ particles extracted from dynamic videos are presented in Figure 5b. It could be seen that upon contact with $KMnO_4$ particles, the BOPA-CHO-embedded sponge immediately shows blue fluorescence emission regardless of the particle size, and all of the fluorescence areas increase with time due to the dissolution and diffusion of the $KMnO_4$ particles. In addition, the fluorescence areas become larger and brighter for $KMnO_4$ particles with greater sizes. The statistical analysis of the relationship between the diffusion diameter and time shows that the large $KMnO_4$ microparticulate with a mass of ~430.3 ng diffused from an initial diameter of 102.7 to 709.0 μm within 20 s, while the diffusion of the small $KMnO_4$ particle with a mass of ~11.6 ng diffused from 30.8 to 390.5 μm (Figure S48). It is worth noting that the mass of a single $KMnO_4$ particle was estimated from the approximate spherical size of the initial blue fluorescence, and the corresponding time was defined as 0 s. Furthermore, the relationship between the diffusion diameter at 25 s and the $KMnO_4$ particle mass was investigated (Figure 5c). It could be seen that with the increase of the $KMnO_4$ particle mass, the increase of the final diffusion diameter slows down gradually. It is found that there is an exponential relationship between the particle mass and the diffusion diameter, demonstrating the reliability of this method for the detection of $KMnO_4$ particles.

To further evaluate the reliability of the test pen in sensing $KMnO_4$ residues in complex environments, test samples were prepared with 10, 5, and 1% mass ratios of $KMnO_4$ in mixing with soil in pot culture, respectively. The tip of the test pen can immediately emit blue fluorescence, and the intensity decreases with the decrease of the $KMnO_4$ ratio (Figure 5d). Especially with a $KMnO_4$ ratio of 1%, the intrinsic blue emission brought by $KMnO_4$ could still be clearly observed, indicating good anti-interference and high reliability of the designed test pen for the rapid discrimination of $KMnO_4$ residues in complex scenarios. Furthermore, this test pen was applied in the simulated test for trace $KMnO_4$ residues (Figure 5e). The trace $KMnO_4$ solid residue samples with masses of 1580, 790, 316, 158, and 79 ng were prepared on glass plates by solvent evaporation of 10 μL of low-concentration $KMnO_4$ solutions (1, 0.5, 0.2, 0.1, and 0.05 mM). After wipe sampling, the $KMnO_4$ particles adhering to the surface of the gloves (1266, 633, 253, 127, and 63 ng/cm^2) were tested with the test pen, and the sensing units could emit bright blue fluorescence with $KMnO_4$ residues above 633 ng/cm^2. With the decrease of the content of the $KMnO_4$ residue below 633 ng/cm^2, the emission gradually weakens. Especially the characteristic fluorescence can still be observed for $KMnO_4$ residues of 63 ng/cm^2. In addition, the test pen can also realize the detection of dissolved $KMnO_4$ in the actual samples, such as soil and wastewater, and the characteristic fluorescence can be observed for 0.1 mM $KMnO_4$ solution sprayed in the soil and 0.2 mM

https://doi.org/10.1021/acs.analchem.3c01120
Anal. Chem. 2023, 95, 9014−9024

$KMnO_4$ in wastewater (Figures S49 and S50), implying that the test pen is highly promising for ultratrace $KMnO_4$ solid and solution residue tracking and discrimination. Compared with the previously reported practical applications for $KMnO_4$ detection, the sponge-based test pen has the superiorities of low cost, convenient sampling, simple operation, and can realize the detection of different forms of target analytes and shows the innovation of the ingenious design (Table S3).

CONCLUSIONS

In summary, we demonstrated that the precise modulation of the electron-withdrawing strength of the substituent, which is located at the *para*-position of the recognition group, is of great significance for regulating the sensing performances of the ESIPT-based probes. Four BOPA-based ESIPT probes were prepared by linking the acryloyl group, which is the recognition site of $KMnO_4$, to the proton donor of the HBO fluorophore, and introducing −F, −CHO, −H, and $-CH_3$ as the electron-withdrawing groups in the *para*-position of the acryloyl group. It has been demonstrated that the largest change of electron transition energy, oscillator strength, and the maximum reactivity of the probe BOPA-CHO, as well as the most stable resulting fluorescent product, together make probe BOPA-CHO the most favorable model molecule. Compared with probes BOPA-F, BOPA-H, and BOPA-CH_3, probe BOPA-CHO showed excellent sensing performances for the detection of $KMnO_4$ with an ultralow detection limit (0.96 nM), rapid response (<3 s), and excellent selectivity even in the presence of 21 interferents. In addition, this probe design has been proven to be reliable to track and discriminate trace $KMnO_4$ solution, particles, and residues in complex scenarios through the fabrication of a BOPA-CHO-embedded sponge-based test pen, which is a groundbreaking advance for on-site $KMnO_4$ detection. The present systematical investigation from both experimental and theoretical basis would definitely set an example for the exploration of ESIPT-based probes and the high-performance detection methodology design toward trace hazardous substances. More importantly, it would help to promote the development of chemical science, molecular engineering, as well as advanced sensing technology, and other fields.

ASSOCIATED CONTENT

Supporting Information

The Supporting Information is available free of charge at https://pubs.acs.org/doi/10.1021/acs.analchem.3c01120.

Synthesis process of probes, preparation of the probe solutions, and the testing process; preparation and testing of the BOPA-CHO-embedded sponge sensor unit for $KMnO_4$ solution and particles; preparation and testing of the BOPA-CHO-embedded sponge-based test pen for $KMnO_4$ residue detection; computational details; H-bond length (Å), potential energy density ρ (BCP), and bond energy (kcal/mol) of intramolecular hydrogen bonds of four probe reaction products by AIM topology analysis; calculated oscillator strength for a low-lying singlet state; emission wavelength (with comparison to the experimental value) and excitation energy of the probes and their reaction products; and comparison of the recently developed optical methods for the detection of $KMnO_4$ (PDF)

AUTHOR INFORMATION

Corresponding Authors

Zhenzhen Cai − *Xinjiang Key Laboratory of Explosives Safety Science, Xinjiang Technical Institute of Physics and Chemistry, Chinese Academy of Sciences, Urumqi 830011, China*; Email: caizz@ms.xjb.ac.cn

Shuhai Zhang − *School of Environment and Safety Engineering, North University of China, Taiyuan 030051, China*; Email: zsh93y@nuc.edu.cn

Xincun Dou − *School of Environment and Safety Engineering, North University of China, Taiyuan 030051, China; Xinjiang Key Laboratory of Explosives Safety Science, Xinjiang Technical Institute of Physics and Chemistry, Chinese Academy of Sciences, Urumqi 830011, China; Center of Materials Science and Optoelectronics Engineering, University of Chinese Academy of Sciences, Beijing 100049, China*; orcid.org/0000-0001-5825-9937; Email: xcdou@ms.xjb.ac.cn

Authors

Yanwen Guo − *School of Environment and Safety Engineering, North University of China, Taiyuan 030051, China*

Fei Yan − *Xinjiang Key Laboratory of Explosives Safety Science, Xinjiang Technical Institute of Physics and Chemistry, Chinese Academy of Sciences, Urumqi 830011, China*

Da Lei − *Xinjiang Key Laboratory of Explosives Safety Science, Xinjiang Technical Institute of Physics and Chemistry, Chinese Academy of Sciences, Urumqi 830011, China*

Yanan Guo − *Xinjiang Key Laboratory of Explosives Safety Science, Xinjiang Technical Institute of Physics and Chemistry, Chinese Academy of Sciences, Urumqi 830011, China*

Complete contact information is available at: https://pubs.acs.org/10.1021/acs.analchem.3c01120

Author Contributions

The manuscript was written through contributions of all authors. All authors have given approval to the final version of the manuscript.

Notes

The authors declare no competing financial interest.

ACKNOWLEDGMENTS

This work was supported by the National Natural Science Foundation of China (22174159, 52172168, 61971416), Youth Innovation Promotion Association of the Chinese Academy of Sciences (2022441), International Science and Technology Cooperation Program of Xinjiang Province (2022E01016), the Key Research Program of Frontier Science, Chinese Academy of Sciences (CAS; Grant No. ZDBS-LY-JSC029), the Natural Science Foundation of Xinjiang Province (2022D01E03), and the Tianshan Talents (2022TSYCCX0074).

REFERENCES

(1) Hobza, P.; Rezac, J. *Chem. Rev.* **2016**, *116*, 4911−4912.
(2) Relph, R. A.; Guasco, T. L.; Elliott, B. M.; Kamrath, M. Z.; McCoy, A. B.; Steele, R. P.; Schofield, D. P.; Jordan, K. D.; Viggiano, A. A.; Ferguson, E. E.; Johnson, M. A. *Science* **2010**, *327*, 308−312.
(3) Gong, Y. J.; Zhang, Y. F.; Xiong, W.; Zhang, K.; Che, Y. K.; Zhao, J. C. *J. Am. Chem. Soc.* **2017**, *139*, 10649−10652.

(4) Liang, M. D.; Li, Z. L.; Wang, W. S.; Liu, J. K.; Liu, L. S.; Zhu, G. L.; Karthik, L.; Wang, M.; Wang, K. F.; Wang, Z.; Yu, J.; Shuai, Y.; Yu, J.; Zhang, L.; et al. *Nat. Commun.* **2019**, *10*, No. 3672.
(5) Sar, D.; Ostadhossein, F.; Moitra, P.; Alafeef, M.; Pan, D. *Adv. Sci.* **2022**, *9*, No. 2202414.
(6) Wang, S. C.; Shi, H.; Wang, L. S.; Loredo, A.; Bachilo, S. M.; Wu, W.; Tian, Z.; Chen, Y. D.; Weisman, R. B.; Zhang, X. J.; Cheng, Z.; Xiao, H. *J. Am. Chem. Soc.* **2022**, *144*, 23668−23676.
(7) Knebel, A.; Caro, J. *Nat. Nanotechnol.* **2022**, *17*, 911−923.
(8) Wang, Y. H.; Shao, Z. S.; Cheng, C.; Wang, J. L.; Song, Z.; Song, W. J.; Zheng, F.; Wang, H. S. *Chem. Eng. J.* **2022**, *437*, No. 135296.
(9) de Arquer, F. P. G.; Talapin, D. V.; Klimov, V. I.; Arakawa, Y.; Bayer, M.; Sargent, E. H. *Science* **2021**, *373*, No. eaaz8541.
(10) Qiu, X. C.; Zhu, X. J.; Su, X. L.; Xu, M.; Yuan, W.; Liu, Q. Y.; Xue, M.; Liu, Y. W.; Feng, W.; Li, F. Y. *Adv. Sci.* **2019**, *6*, No. 1801834.
(11) Zhang, J.; Hou, J. J.; Zhang, K.; Zhang, R. L.; Geng, J. L.; Wang, S. H.; Zhang, Z. P. *J. Hazard. Mater.* **2022**, *436*, No. 129182.
(12) Liu, X. H.; Zhang, Q. W.; Knoll, W.; Liedberg, B.; Wang, Y. *Adv. Mater.* **2020**, *32*, No. 2000866.
(13) Quan, Z. Y.; Xue, F.; Li, H. Y.; Chen, Z. P.; Wang, L.; Zhu, H. X.; Pang, C. L.; He, H. *Chem. Eng. J.* **2022**, *431*, No. 133954.
(14) Shen, J.; Xiao, Q.; Sun, P.; Feng, J.; Xin, X.; Yu, Y.; Qi, W. *ACS Nano* **2021**, *15*, 4947−4955.
(15) Cheng, X.; Sun, P.; Zhang, N.; Zhou, S.; Xin, X. *J. Mol. Liq.* **2021**, *323*, No. 115032.
(16) Chen, N.; Du, N.; Wang, W.; Liu, T.; Yuan, Q.; Yang, Y. *Angew. Chem., Int. Ed.* **2022**, *61*, No. e202115572.
(17) Liu, G.; Wei, J.; Li, X.; Tian, M.; Wang, Z.; Shen, C.; Sun, W.; Li, C.; Li, X.; Lv, E.; Tian, S.; Wang, J.; Xu, S.; Zhao, B. *Adv. Sci.* **2022**, *9*, No. 2202505.
(18) Yu, X. T.; Gong, Y. J.; Ji, H. W.; Cheng, C. Q.; Lv, C. X.; Zhang, Y. F.; Zang, L.; Zhao, J. C.; Che, Y. K. *ACS Sens.* **2022**, *7*, 1395−1402.
(19) Zeng, Y.; Dou, T. T.; Ma, L.; Ma, J. W. *Adv. Sci.* **2022**, *9*, No. 2202384.
(20) Zhang, L.; Chu, M. G.; Ji, C. L.; Wang, W. J.; Tan, J.; Yuan, Q. *Sci. China Chem.* **2023**, *66*, 388−405.
(21) Zhang, Y.; Feng, N.; Zhou, S.; Xin, X. *Nanoscale* **2021**, *13*, 4140−4150.
(22) Wang, W.; Wang, Z.; Sun, D.; Li, S.; Deng, Q.; Xin, X. *Nanomaterials* **2022**, *12*, 424.
(23) Ke, Y. L.; Liu, Y.; Zu, B. Y.; Lei, D.; Wang, G. F.; Li, J. G.; Ren, W. F.; Dou, X. C. *Angew. Chem., Int. Ed.* **2022**, *61*, No. e202203358.
(24) Qiao, Q.; Liu, W.; Chen, J.; Wu, X.; Deng, F.; Fang, X.; Xu, N.; Zhou, W.; Wu, S.; Yin, W.; Liu, X.; Xu, Z. *Angew. Chem., Int. Ed.* **2022**, *61*, No. e202202961.
(25) Xiao, F. F.; Li, Y. S.; Li, J. G.; Lei, D.; Wang, G. F.; Zhang, T. S.; Hu, X. Y.; Dou, X. C. *Aggregate* **2022**, *3*, No. e260.
(26) Wu, L.; Sedgwick, A. C.; Sun, X.; Bull, S. D.; He, X. P.; James, T. D. *Acc. Chem. Res.* **2019**, *52*, 2582−2597.
(27) Ferreira, R. B.; Fu, L.; Jung, Y.; Yang, J.; Carroll, K. S. *Nat. Commun.* **2022**, *13*, No. 5522.
(28) Xu, H.; Xu, H.; Ma, S. N.; Chen, X. N.; Huang, L. X.; Chen, J. W.; Gao, F.; Wang, R.; Lou, K. Y.; Wang, W. *J. Am. Chem. Soc.* **2018**, *140*, 16408−16412.
(29) Berenbeim, J. A.; Boldissar, S.; Owens, S.; Haggmark, M. R.; Gate, G.; Siouri, F. M.; Cohen, T.; Rode, M. F.; Patterson, C. S.; de Vries, M. S. *Sci. Adv.* **2019**, *5*, No. eaaw5227.
(30) Chen, Y. H.; Lee, Y. R.; Wang, W. J.; Fang, Y.; Lu, S.; Han, J. J.; Chen, X. Q.; Kim, M. H.; Yoon, J. Y. *Angew. Chem., Int. Ed.* **2023**, *62*, No. e202301765.
(31) Kim, D.; Jeong, K.; Kwon, J. E.; Park, H.; Lee, S.; Kim, S.; Park, S. Y. *Nat. Commun.* **2019**, *10*, No. 3089.
(32) Shukla, A.; Mai, V. T. N.; Divya, V. V.; Suresh, C. H.; Paul, M.; Karunakaran, V.; McGregor, S. K. M.; Allison, I.; Narayanan Unni, K. N.; Ajayaghosh, A.; Namdas, E. B.; Lo, S. C. *J. Am. Chem. Soc.* **2022**, *144*, 13499−13510.
(33) Li, J. G.; Lei, D.; Ma, Z. W.; Zu, B. Y.; Dou, X. C. *J. Phys. Chem. Lett.* **2022**, *13*, 10871−10881.
(34) Sedgwick, A. C.; Dou, W. T.; Jiao, J. B.; Wu, L.; Williams, G. T.; Jenkins, A. T. A.; Bull, S. D.; Sessler, J. L.; He, X. P.; James, T. D. *J. Am. Chem. Soc.* **2018**, *140*, 14267−14271.
(35) Sedgwick, A. C.; Wu, L. L.; Han, H. H.; Bull, S. D.; He, X. P.; James, T. D.; Sessler, J. L.; Tang, B. Z.; Tian, H.; Yoon, J. Y. *Chem. Soc. Rev.* **2018**, *47*, 8842−8880.
(36) Padalkar, V. S.; Seki, S. *Chem. Soc. Rev.* **2016**, *45*, 169−202.
(37) Ma, Z. W.; Li, J. G.; Hu, X. Y.; Cai, Z. Z.; Dou, X. C. *Adv. Sci.* **2020**, *7*, No. 2002991.
(38) Yang, W. Y.; Lai, R. C.; Wu, J. J.; Yu, Y. J.; Yan, C. C.; Sun, C. F.; Wang, X. D.; Liao, L. S. *Adv. Funct. Mater.* **2022**, *32*, No. 2204129.
(39) Hwang, S. H.; Kim, H.; Ryu, H.; Serdiuk, I. E.; Lee, D. W.; Choi, T. L. *J. Am. Chem. Soc.* **2022**, *144*, 1778−1785.
(40) Göbel, D.; Duvinage, D.; Stauch, T.; Nachtsheim, B. J. *J. Mater. Chem. C* **2020**, *8*, 9213−9225.
(41) Zhang, Q.; Yang, L.; Han, Y.; Wang, Z. Y.; Li, H. J.; Sun, S. G.; Xu, Y. Q. *Chem. Eng. J.* **2022**, *428*, No. 130986.
(42) Kyriukha, Y. A.; Kucherak, O. A.; Yushchenko, T. I.; Shvadchak, V. V.; Yushchenko, D. A. *Sens. Actuators, B* **2018**, *265*, 691−698.
(43) Göbel, D.; Rusch, P.; Duvinage, D.; Bigall, N. C.; Nachtsheim, B. J. *Chem. Commun.* **2020**, *56*, 15430−15433.
(44) Liu, Y.; Li, J. G.; Wang, G. F.; Zu, B. Y.; Dou, X. C. *Anal. Chem.* **2020**, *92*, 13980−13988.
(45) Wang, G. F.; Wan, Z. X.; Cai, Z. Z.; Li, J. G.; Li, Y. S.; Hu, X. Y.; Lei, D.; Dou, X. C. *Anal. Chem.* **2022**, *94*, 11679−11687.
(46) Yang, X. Y.; Cai, Z. Z.; Li, D. Z.; Lei, D.; Li, Y. S.; Wang, G. F.; Zhang, J.; Dou, X. C. *Anal. Chem.* **2022**, *94*, 9184−9192.
(47) Shi, G.; Shahid, M. A.; Yousuf, M.; Mahmood, F.; Rasheed, L.; Bielawski, C. W.; Kim, K. S. *Chem. Commun.* **2019**, *55*, 1470−1473.
(48) Guo, L. J.; Yang, Z.; Dou, X. C. *Adv. Mater.* **2017**, *29*, No. 1604528.
(49) Wu, Z. F.; Zhou, C. Y.; Zu, B. Y.; Li, Y. S.; Dou, X. C. *Adv. Funct. Mater.* **2016**, *26*, 4578−4586.
(50) Qu, J.; Ge, Y. R.; Zu, B. Y.; Li, Y. X.; Dou, X. C. *Small* **2016**, *12*, 1369−1377.
(51) Chen, S.; Yu, Y. L.; Wang, J. H. *Anal. Chim. Acta* **2018**, *999*, 13−26.
(52) Baheti, A.; Vigalok, A. *J. Am. Chem. Soc.* **2019**, *141*, 12224−12228.
(53) Zhu, K.; Fan, R. Q.; Zheng, X. B.; Wang, P.; Chen, W.; Sun, T. C.; Gai, S.; Zhou, X. S.; Yang, Y. L. *J. Mater. Chem. C* **2019**, *7*, 15057−15065.
(54) Du, F. F.; Li, G.; Gong, X. J.; Guo, Z. H.; Shuang, S. M.; Xian, M.; Dong, C. *Sens. Actuators, B* **2018**, *277*, 492−501.
(55) Ding, P.; Xin, X.; Zhao, L. L.; Xie, Z. C.; Zhang, Q. H.; Jiao, J. M.; Xu, G. Y. *RSC Adv.* **2017**, *7*, 3051−3058.
(56) Zhou, Z. Q.; Liao, Y. P.; Wu, H. Y.; Xiao, Q.; Liu, Y.; Yang, L. Y. *Microporous Mesoporous Mater.* **2022**, *338*, No. 111971.
(57) Suryawanshi, S. B.; Mahajan, P. G.; Bhopate, D. P.; Kolekar, G. B.; Patil, S. R.; Bodake, A. J. *J. Photochem. Photobiol. A* **2016**, *329*, 255−261.
(58) Li, N.; Huang, J. X.; Wang, Q. Q.; Gu, Y. Q.; Wang, P. *Sens. Actuators, B* **2018**, *254*, 411−416.
(59) Yang, X.; Qin, X.; Li, Y.; Yan, M.; Cui, Y.; Sun, G. *Biosens. Bioelectron.* **2018**, *121*, 62−71.
(60) Niu, L.; Zhang, T.; Zhao, H.; Dong, H.; Zhang, Y.; Liang, T.; Wang, J. *Dyes Pigm.* **2022**, *206*, No. 110610.
(61) Dai, Y.; Xue, T.; Zhang, X.; Misal, S.; Ji, H.; Qi, Z. *Spectrochim. Acta, Part A* **2019**, *216*, 365−374.
(62) Kaur, H.; Walia, S.; Karmakar, A.; Krishnan, V.; Koner, R. R. *J. Environ. Chem. Eng.* **2022**, *10*, No. 106667.
(63) Zhu, K.; Fan, R.; Zheng, X.; Wang, P.; Chen, W.; Sun, T.; Gai, S.; Zhou, X.; Yang, Y. *J. Mater. Chem. C* **2019**, *7*, 15057−15065.
(64) Ding, C. H.; Deng, Z. Q.; Chen, J. C.; Jin, Y. Z. *Colloids Surf., B* **2020**, *189*, No. 110838.

https://doi.org/10.1021/acs.analchem.3c01120
Anal. Chem. 2023, 95, 9014−9024

(65) Sun, P.; Zhang, S.; Xiang, Z.; Zhao, T.; Sun, D.; Zhang, G.; Chen, M.; Guo, K.; Xin, X. *J. Colloid Interface Sci.* **2019**, *547*, 60−68.
(66) Wu, J. X.; Yan, B. *J. Colloid Interface Sci.* **2017**, *504*, 197−205.

https://doi.org/10.1021/acs.analchem.3c01120
Anal. Chem. 2023, 95, 9014−9024